



ELSEVIER

Available online at [www.sciencedirect.com](http://www.sciencedirect.com)

jmr&t  
Journal of Materials Research and Technology

journal homepage: [www.elsevier.com/locate/jmrt](http://www.elsevier.com/locate/jmrt)



# The improvement of room temperature plasticity of refractory high entropy alloy based on different first principles calculation models and experiment verification

Yu Gao <sup>a,b</sup>, Kai Chong <sup>b</sup>, Chang Liu <sup>b</sup>, Yingwen Cao <sup>c</sup>, Ting Xue <sup>b</sup>,  
Fuqiang Guo <sup>b,\*</sup>, Yong Zou <sup>d,\*\*</sup>

<sup>a</sup> Shenzhen Research Institute of Shandong University, Shenzhen, 518063, China

<sup>b</sup> Key Laboratory of Liquid-Solid Structural Evolution and Processing of Materials, Ministry of Education, Shandong University, Jinan, Shandong, 250061, China

<sup>c</sup> School of Materials and Chemical Engineering, Ningbo University of Technology, Ningbo, 315211, China

<sup>d</sup> Shandong Engineering & Technology Research Center for Modern Welding, Shandong University, Jinan, Shandong, 250061, China

## ARTICLE INFO

### Article history:

Received 6 June 2023

Accepted 16 August 2023

Available online 22 August 2023

### Keywords:

Refractory high entropy alloys

First principles calculation

Elastic properties

Electronic structure

## ABSTRACT

The limited ductility of Refractory High Entropy Alloy (RHEA) at room temperature hinders its widespread application. However, optimizing their properties through traditional “trial and error” methods is a challenging due to the intricate composition of High Entropy Alloys (HEAs). First principles calculation is an efficient and cost-effective method for predicting material properties. Three modeling methods for high entropy alloys are the most commonly used, namely Supercell (SC), Special quasi-random structure (SQS) and Virtual crystal approximation (VCA). To improve the plasticity of NbMoTaTiV at room temperature, the effects of Ti and Ta contents on the mechanical properties were studied. First principles calculations have been employed to predict the phase structure, elastic properties and electronic structure by three common modeling methods and validated against experimental data. The result revealed that MoNbTaTiV and MoNbTa<sub>0.5</sub>Ti<sub>1.5</sub>V RHEAs have BCC structure and increasing Ti and decreasing Ta contributed to enhanced toughness of the alloy. Notably, the three methods demonstrated good accuracy in predicting the effects of Ti and Ta content on the performance of NbMoTaTiV. The VCA method was particularly well-suited for predicting elastic properties, offering a balance between computational accuracy and efficiency. SQS and SC considered the complex atomic occupation in HEAs, making them more suitable for studying the electronic structure.

© 2023 The Authors. Published by Elsevier B.V. This is an open access article under the CC BY-NC-ND license (<http://creativecommons.org/licenses/by-nc-nd/4.0/>).

\* Corresponding author.

\*\* Corresponding author.

E-mail addresses: [201813745@mail.sdu.edu.cn](mailto:201813745@mail.sdu.edu.cn) (F. Guo), [yzou@sdu.edu.cn](mailto:yzou@sdu.edu.cn) (Y. Zou).

<https://doi.org/10.1016/j.jmrt.2023.08.149>

2238-7854/© 2023 The Authors. Published by Elsevier B.V. This is an open access article under the CC BY-NC-ND license (<http://creativecommons.org/licenses/by-nc-nd/4.0/>).

## 1. Introduction

High entropy alloys (HEAs) represent a novel alloy, with each component ranging between 5 at.% and 35 at.% [1,2]. HEA exhibited four essential effects: the high-entropy effect, the lattice distortion effect, the sluggish diffusion effect, and the cocktail effect [3,4]. A variety of exceptional properties have been facilitated by these effects, which include outstanding mechanical properties [5–7], excellent wear resistance [8–10], impressive oxidation resistance [11,12], corrosion resistance [7,13], etc. It is worth mentioning that HEAs can be classified into two distinct categories based on their different elemental compositions: the transition high entropy alloys (THEAs), and the refractory high entropy alloys (RHEAs) [14].

RHEAs, a concept proposed by Senkov in 2010 [15,16], were inspired by the goal of developing innovative high-temperature structural metals as the urgent demand for superalloys in the aerospace sector. As technological advancements push the boundaries, operating temperature in various applications have gradually approached the melting point of nickel-based superalloy and cobalt-based superalloy. Consequently, the traditional superalloys have reached their limits in meeting the requirements of high temperature protection in the aerospace industry. RHEAs have attracted increasing attention within the aeronautics field owing to their unique high temperature properties [17]. Typically, RHEAs comprised element with high melting point [14]. Nowadays, reported RHEAs were predominantly based on element groupings like MoNbTaW or HfNbTaZr [18]. MoNbTaW and MoNbTaVW had remarkable mechanical properties at high temperature, boasting an impressive yield strength exceeding 400 MPa at 1600 °C [15,16]. Nonetheless, MoNbTaW and MoNbTaVW RHEAs exhibit limited ductile and density at room temperature. Furthermore, various RHEAs have been extensively studied. For instance, the compressive yield strength of CrMo<sub>0.5</sub>NbTa<sub>0.5</sub>TiZr RHEA at room temperature was 1595 MPa, the fracture strength was 2000 MPa, but the compressive plasticity was limited to only 5% [19]. The TaNbHfZr RHEA displayed an outstanding yield strength of 2310 MPa following annealing, but the compressive fracture strain was a mere 0.35% [20]. Guo et al. prepared the NbTaWMoSi<sub>x</sub> ( $x = 0, 0.25, 0.5, 0.75$ ) RHEAs by spark plasma sintering [21]. The fracture strain showed a non-linear trend with the increase of Si content, initially rising and then decreasing. To improve room temperature ductility and reduce the density, Senkov replaced W, Mo, and V (heavier elements) with Hf, Zr, and Ti (lighter elements) and first synthesized TaNbHfZrTi [18]. The TaNbHfZrTi alloy demonstrated improved ductility, albeit at the expense of a reduced yield strength of 92 MPa at 1200 °C [22]. Since then, the researchers have focused on designing the RHEAs based on the MoNbTaW or HfNbTaZr compositions, aiming to achieve a balance between room temperature toughness and high temperature mechanical properties through modifications of element content and composition.

High Entropy Alloys (HEAs) are characterized by a wide range of components and intricate alloying rules, making traditional “trial-and-error” methods impractical, especially given the high cost of refractory elements involved.

HEA has a wide range of components and complex alloying rules, making traditional “trial-and-error” method impractical, especially given the high cost of refractory elements involved. Therefore, computational simulation has become an effective method for designing composition and investigating properties research of RHEAs. Among these simulations, the first principles calculation has been widely employed to optimal alloy performance. For HEAs, the establishment of appropriate initial configuration is the premise to predict the crystal structure and properties. At present, several commonly used modeling methods mainly include Virtual crystal approximation (VCA) [23,24], Coherent potential approximation (CPA) [25], Special quasi-random structure (SQS) [26], Supercell (SC) [27] and so on. Tong and Hu et al. [27–29] established first-principles calculations through SC and VCA, focusing on how Ti and Mo elements influence the structure, electronic and elastic properties of NbMoTaW based RHEAs. The conclusions well agreed with the experimental result. Liu et al. [30] constructed SQS model to explore the effect of alloying on NbMoTaWM, where M is Cr, V, Ti, Zr or Hf. Bhandari et al. [31] studied Mo<sub>20</sub>Nb<sub>20</sub>Re<sub>20</sub>Ta<sub>20</sub>W<sub>20</sub>, Mo<sub>15</sub>Nb<sub>20</sub>Re<sub>15</sub>Ta<sub>30</sub>W<sub>20</sub> and Mo<sub>15</sub>Nb<sub>20</sub>Re<sub>10</sub>Ta<sub>35</sub>W<sub>20</sub> RHEAs, ultimately selecting Mo<sub>15</sub>Nb<sub>20</sub>Re<sub>15</sub>Ta<sub>30</sub>W<sub>20</sub> to compare experimental exploration with computational predictions. Yao et al. [32] study the MoNbTaTiV RHEA by CALPHAD method and first-principles calculation. MoNbTaTiV has lower density and higher room temperature toughness than that of MoNbTaW and MoNbTaVW, which was expected to be utilized as a potential high temperature structural material. Despite these advantageous properties, there has been limited research conducted on these alloys [33]. Hence, enhancing Ti content and reducing Ta content are expected to further improve the toughness and reduce the density. Besides, a comprehensive evaluation of the accuracy and efficiency of different first-principles modeling approaches for HEAs remains relatively unexplored, warranting further investigation in this critical area of materials research.

This paper was focused on the NbMoTaTiV-based RHEAs, which investigate the influence of Ti and Ta contents on mechanical properties and electronic structures. The elastic properties, lattice constants and electronic properties of NbMoTaTiV and NbMoTa<sub>0.5</sub>Ti<sub>1.5</sub>V were predicted through the first principle calculation build by different models. By comparing the three modelling methods, their accuracy was evaluated and potential sources of error were analyzed. Furthermore, the calculated results were verified by experimental data. The NbMoTaTiV and NbMoTa<sub>0.5</sub>Ti<sub>1.5</sub>V RHEAs were prepared by vacuum arc melting, conducting a comprehensive tests of phase composition, microstructure and mechanical properties.

## 2. Methods

### 2.1. Computational methods

For HEAs of first principles calculation, establishing an appropriate initial configuration is crucial. Among them, commonly used modeling methods mainly include SC, SQS and VCA. Considering the characteristics of disordered solid

solution of HEA, SC initiates from the single cell, randomizing and expanding different elements. SQS utilizes Monte Carlo algorithm to optimize SC model based on correlation function. VCA, in contrast, revolves around replacing real components in the solution disordered alloy with virtual mixed atoms, but its applicability is limited to HEAs with similar chemical properties.

In this study, Density Function Theory (DFT) was employed for theoretical calculation, utilizing three commonly used first-principle methods, namely SC, SQS, and VCA. Among them, the BCC SQS structures with 100 disordered atoms were generated for each composition using the alloy theoretic automation toolkit (ATAT) code. The generalized-gradient approximation of Perdew–Burke–Ernzerhof was adopted to describe the exchange-correlation function. The Monkhorst–Pack methods were employed for K points ( $1 \times 1 \times 2$ ) in the Brillouin zone. The unoptimized SQS supercell models of MoNbTaTiV and MoNbTa<sub>0.5</sub>Ti<sub>1.5</sub>V RHEAs are shown in Fig. 1(a)–(b). In the SC method, the supercell containing 10 atoms was created as Fig. 1 (c)–(d). For VCA, the single cell with mixed atoms was built as Fig. 1 (e). Through the convergence test, the cutoff energy of both SC and VCA models was set to 1200 eV, and the K points of SC and VCA were  $10 \times 10 \times 2$  and  $16 \times 16 \times 16$  respectively. To verify the accuracy of parameters, the lattice parameters of single-phase BCC MoNbTaTiV RHEA was calculated to be 3.183 Å by SQS, 3.226 Å by SC and 3.223 Å by VCA, which was well agreed with

the calculated value (3.218 Å) and the experimental value (3.224 Å) by Yao [32]. The excellent agreement between the parameters obtained from different models and the reported values further validates the rationality of the calculation process.

## 2.2. Experimental

A mixture of 99.5% pure metal powders with a weight of 30 g was cold-pressed into slices using a graphite die with a diameter of 20 mm. Subsequently, the ingots were synthesized by melted the cold-pressed slices. The vacuum arc melting furnace was used to melt with a vacuum of  $5 \times 10^{-3}$  Pa. To ensure uniform composition and structure, the alloy ingots underwent five rounds of melting. The sample of NbMoTaTiV and NbMoTa<sub>0.5</sub>Ti<sub>1.5</sub>V RHEAs were wet-grinded with SiC emery papers from 400# to 2000# and then use the 2.0 μm diamond polish mechanical polishing more than 5 min. The X-ray diffraction (DX2700, China) was used to analyze the samples' structure with Cu Ka radiation source and the scan rate and range were set as 10°/min and 20°–90°. The field-emission scanning electron microscope (JEOL JSM-7800 F, Japan) with the energy dispersive X-ray spectroscopy (EDS) was used to analyze the properties of microstructure and chemical composition. A Vickers hardness tester was used to measure the microhardness of the NbMoTaTiV and NbMoTa<sub>0.5</sub>Ti<sub>1.5</sub>V alloy, applying a test load of 200g for 15s. The

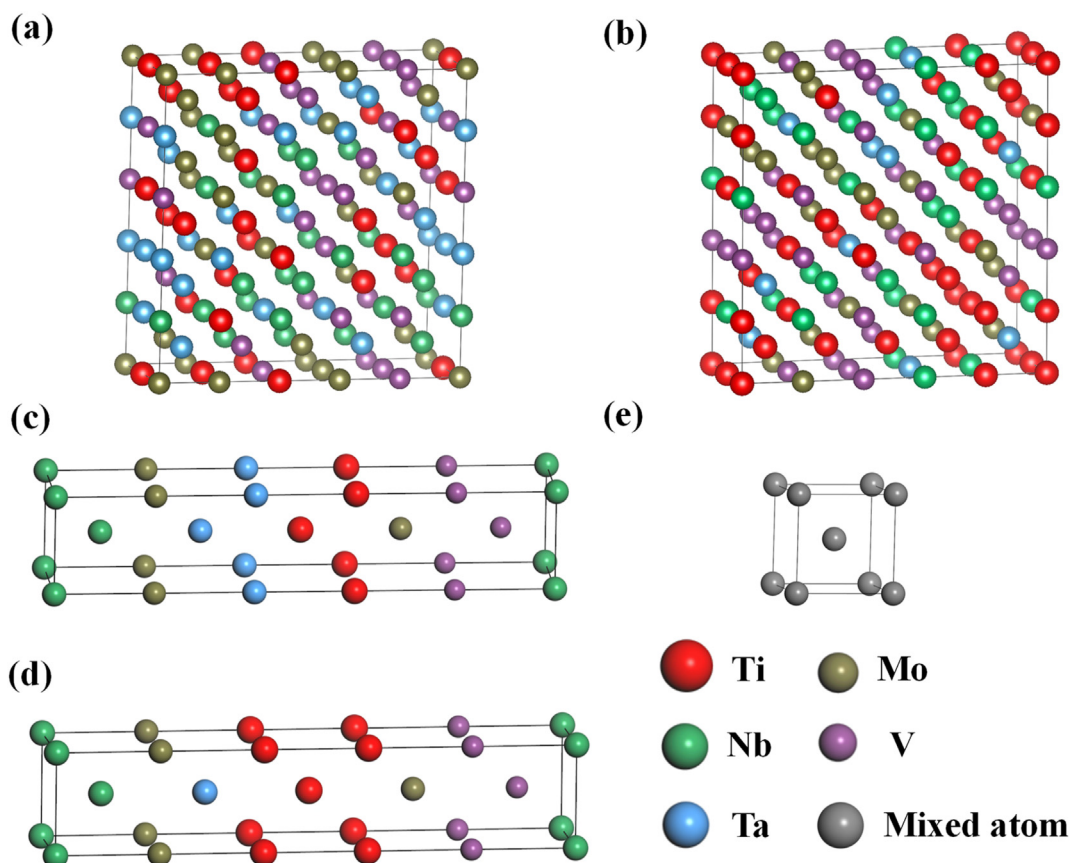


Fig. 1 – The unoptimized SQS supercell models, SC model and VCA model. (a) NbMoTaTiV SQS model; (b) NbMoTa<sub>0.5</sub>Ti<sub>1.5</sub>V SQS model; (c) NbMoTaTiV SC model; (d) NbMoTa<sub>0.5</sub>Ti<sub>1.5</sub>V SC model; (e) BCC model built by VCA.

microhardness was calculated by taken the average value of five different test points. Additionally, the density of the sample was measured through the Archimede drainage method. The elastic modulus of NbMoTaTiV and NbMoTa<sub>0.5</sub>Ti<sub>1.5</sub>V alloy were tested through the ultrasonic method (TECLAB UMS-100, France). The sample of UMS size was 5 × 5 × 2 mm and the surfaces were polished and kept parallel. The universal testing machine (Zwick/Roell Z250) was used to carry out the compression test at room temperature with a strain rate set at 0.001 s<sup>-1</sup>. The test sample was taken from the core of the ingot and the size is Φ3.6 × 5.4 mm.

### 3. Result and discussion

#### 3.1. Phase structure

To predict phase structure of HEA, many researchers have proposed a series of empirical formulas. The most representative of the empirical formulas to predict solid solution phase formation of HEAs were atomic size difference ( $\delta$ ), valence electron concentration (VEC), the entropy ( $\Delta S_{\text{mix}}$ ), enthalpy of mixing ( $\Delta H_{\text{mix}}$ ), electronegativity criterion ( $\chi$ ) and so on. The theoretical criterion for phase structure of NbMoTaTiV and NbMoTa<sub>0.5</sub>Ti<sub>1.5</sub>V RHEAs were presented in Table 1. According to the literatures [34–40], a solid solution was formed under the condition of  $\Omega \geq 1.1\%$ ,  $\delta \leq 6.6\%$  and  $-15 < \Delta H_{\text{mix}} < 5 \text{ kJ/mol}$ . Besides,  $\text{VEC} < 6.87$  is considered as a stable BCC phase. The empirical formula was listed in Table 1. The table showed that the VEC value for the MoNbTaTiV and MoNbTa<sub>0.5</sub>Ti<sub>1.5</sub>V was below 6.87, and the  $\Omega$  value ranged between 1.1% and 6.6%, suggesting that the MoNbTaTiV and MoNbTa<sub>0.5</sub>Ti<sub>1.5</sub>V were BCC structure steadily.

Besides, M.C. Gao et al. [41] calculated the formation enthalpy ( $H_{\text{form}}$ ) of large number of HEAs, and found that when it was between -8 and 8.5 kJ/mol, single-phase solid solution was often formed. The stability of the crystal was determined by cohesive energy. The lower the cohesive energy ( $E_{\text{coh}}$ ), the more stable the crystals [42]. The total energy ( $E_{\text{tot}}$ ) of relaxed structure could be obtained by the first principle calculation. For the SQS model, the numbers of the supercell were 100 atoms. The  $H_{\text{form}}$  and  $E_{\text{coh}}$  were calculated based on Eqs. (1) and (2) [27,29]:

$$H_{\text{form}} = \frac{1}{N_x} \left( E_{\text{tot}} - \sum n_x E_{\text{solid}}^x \right) \quad (1)$$

$$E_{\text{coh}} = \frac{1}{N_x} \left( E_{\text{tot}} - \sum n_x E_{\text{atom}}^x \right) \quad (2)$$

Here,  $E_{\text{tot}}$  is the total energy of optimized RHEA.  $N_x$  and  $n_x$  represent the atomic numbers of all and every component.

**Table 1 – The theoretical criterion for phase structure of MoNbTaTiV and NbMoTa<sub>0.5</sub>Ti<sub>1.5</sub>V RHEAs.**

Alloys	$\Delta S_{\text{mix}}$ (J/K·mol)	$\Delta H_{\text{mix}}$ (kJ/mol)	$\delta(\%)$	$\Omega$	VEC
NbMoTaTiV	13.38	-2.56	3.54%	13.6	5.0
NbMoTa <sub>0.5</sub> Ti <sub>1.5</sub> V	12.95	-2.44	3.66%	13.1	4.9

$E_{\text{solid}}^x$  is the total energy of average atom in a single crystal cell for every component in Nb–Mo–Ta–Ti–V RHEAs.  $E_{\text{atom}}^x$  is the total energy of isolated atom in a crystal cell. The  $E_{\text{form}}$  and  $E_{\text{coh}}$  of MoNbTaTiV and MoNbTa<sub>0.5</sub>Ti<sub>1.5</sub>V RHEAs were listed in Fig. 2. It could be observed that both  $H_{\text{form}}$  and  $E_{\text{coh}}$  of MoNbTaTiV and MoNbTa<sub>0.5</sub>Ti<sub>1.5</sub>V RHEAs are negative. The  $H_{\text{form}}$  of MoNbTaTiV and NbMoTa<sub>0.5</sub>Ti<sub>1.5</sub>V RHEAs were between -8 kJ/mol and 8.5 kJ/mol. The calculated data indicated that MoNbTaTiV and NbMoTa<sub>0.5</sub>Ti<sub>1.5</sub>V RHEAs should be single phase BCC structure.

#### 3.2. Elastic properties

The use of SQS and SC methods to simulate HEAs often results in a reduction of the structure's symmetry. Nine elastic constants were computed for the relaxed structure, with Table 2 presenting the values for the optimized MoNbTaTiV and MoNbTa<sub>0.5</sub>Ti<sub>1.5</sub>V RHEA using the SQS and SC models. While BCC crystal structures typically possess three independent elastic constants, the SQS and SC models yield nine independent elastic constants. To obtain the mean elastic constants, the data was processed using Eq. (3).

$$C_{11} = \frac{C_{11} + C_{22} + C_{33}}{3}, C_{12} = \frac{C_{12} + C_{23} + C_{13}}{3}, C_{44} = \frac{C_{44} + C'_{55} + C'_{66}}{3} \quad (3)$$

Table 3 presented the mean elastic constants ( $C_{11}$ ,  $C_{12}$ ,  $C_{44}$ ) and elastic properties of MoNbTaTiV and MoNbTa<sub>0.5</sub>Ti<sub>1.5</sub>V RHEAs, which were calculated by SQS, SC and VCA methods. To evaluate the mechanical stability of the cubic system, Eq. (4) was utilized. The calculation of elastic constants using DFT revealed that NbMoTaTiV and NbMoTa<sub>0.5</sub>Ti<sub>1.5</sub>V RHEAs have elastic stability.

$$C_{44} > 0, C_{11} > |C_{12}|, C_{11} + 2C_{12} > 0 \quad (4)$$

In Mo–Nb–Ta–Ti–V RHEAs, the elastic constants ( $C_{11}$ ,  $C_{12}$ ,  $C_{44}$ ) of the material, obtained through three different modeling methods, exhibited a decreasing trend with increasing Ti element content and decreasing Ta element

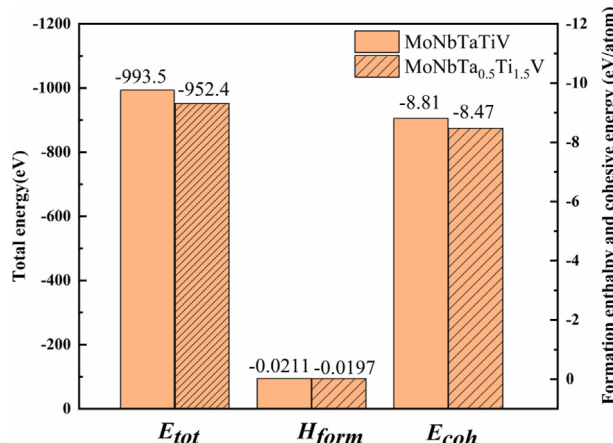


**Fig. 2 – The total energy ( $E_{\text{tot}}$ ), formation enthalpy ( $H_{\text{form}}$ ) and the cohesive energy ( $E_{\text{coh}}$ ) of the MoNbTaTiV and MoNbTa<sub>0.5</sub>Ti<sub>1.5</sub>V RHEAs built by SQS.**

**Table 2 – Nine independent elastic constants (GPa) of relaxed supercell of NbMoTaTiV and NbMoTa<sub>0.5</sub>Ti<sub>1.5</sub>V RHEAs.**

Alloy	C'₁₁ (GPa)	C'₁₂ (GPa)	C'₁₃ (GPa)	C'₂₂ (GPa)	C'₂₃ (GPa)	C'₃₃ (GPa)	C'₄₄ (GPa)	C'₅₅ (GPa)	C'₆₆ (GPa)
NbMoTaTiV-SQS	259.5	124.0.1	120.5	283.8	132.5	281.5	55.4	46.6	47.1
NbMoTaTiV-SC	222.3	126.2	127.0	257.6	143.8	258.5	51.3	29.4	29.5
NbMoTa <sub>0.5</sub> Ti <sub>1.5</sub> V-SQS	248.4	123.0	122.3	249.1	123.0	260.3	44.6	46.4	41.6
NbMoTa <sub>0.5</sub> Ti <sub>1.5</sub> V -SC	219.6	114.7	114.7	275.1	103.5	275.0	46.8	19.2	19.2

content. The elastic constants would directly affect the elastic properties of the material, such as bulk modulus (B), shear modulus (G), Young's modulus (E), and Poisson's ratio ( $\nu$ ). Comparing three different modeling methods, it was observed that the values of B, G and E decrease with decreasing C<sub>11</sub>, C<sub>12</sub>, and C<sub>44</sub>. Notably, the results calculated by SQS in this study are close to those reported for NbMoTaTiV using SQS [32]. The calculation error was mainly due to the difference of the selected supercell model.

In addition, the Poisson's ratio ( $\nu$ ) of the material plays a crucial role in determining the ductility of the material. It represents the material's ability to undergo plastic deformation when subjected to a force. A higher  $\nu$  indicates better the plasticity and higher the ductility. Pugh's criteria [43] suggested that the ratio of shear modulus to bulk modulus B/G could reflect a material's brittleness and toughness, with higher B/G values indicating greater toughness. The critical value B/G = 1.75 serves as a threshold to distinguish between ductile and brittle materials. The material has better toughness properties when B/G is greater than 1.75. Our calculations revealed that both MoNbTaTiV and MoNbTa<sub>0.5</sub>Ti<sub>1.5</sub>V RHEAs had B/G ratio greater than 1.75 and  $\nu$  greater than 0.26. With the increase of Ti and the decrease of Ta,  $\nu$  and B/G both increased, indicating that the ductility of the material was improved.

To ensure the effective utilization of RHEAs as structural materials, understanding the mechanical anisotropy arising from their preparation techniques is crucial. This investigation would offer valuable insights into their future applications. The three-dimensional (3D) surface and the planar projection of Young's modulus of NbMoTaTiV and NbMoTa<sub>0.5</sub>Ti<sub>1.5</sub>V RHEAs were calculated by SQS, SC, and VCA model as shown in Fig. 3. For cubic structures, the 3D representation of Young's modulus is given by Eq. (5).

$$\frac{1}{E} = l_1^4 S_{44} + l_2^4 S_{22} + l_3^4 S_{33} + 2l_1^2 l_2^2 S_{12} + 2l_1^2 l_3^2 S_{13} + 2l_2^2 l_3^2 S_{23} + l_1^2 l_2^2 S_{66} + l_1^2 l_3^2 S_{55} + l_2^2 l_3^2 S_{44} \quad (5)$$

where, S<sub>ij</sub> is elastic compliance constant, through the elastic constant matrix inversion; l<sub>1</sub>, l<sub>2</sub>, and l<sub>3</sub> are the cosine values

along the x, y, and z axes, respectively. For isotropic materials, the idealized shape of the Young's modulus resembles a sphere. The results indicated that NbMoTaTiV and NbMoTa<sub>0.5</sub>Ti<sub>1.5</sub>V RHEAs built by SQS and SC exhibited evident elastic anisotropy. The model based on SC method showed the largest deviation from the sphere. The deviation from the sphere is the largest, indicating the strongest anisotropy in the alloy. This anisotropy obtained by SC could be attributed to the complex interaction and arrangement of different elements in the supercell during computational modeling. Conversely, the model built by VCA exhibited a tendency towards a more spherical shape, indicating a gradual tendency towards isotropy. The projection of Young's modulus on (110) and (001) crystal plane revealed that the anisotropy of Young's modulus on (001) crystal plane was weaker than that on (110). The stiffness of the alloy decreases with the increase of Ti content and the decrease of Ta content.

### 3.3. Electronic structure

To explore the internal mechanism of material structure stability, the density of states of MoNbTaTiV and MoNbTa<sub>0.5</sub>Ti<sub>1.5</sub>V were calculated. The total and partial densities of states were computed and illustrated in Fig. 4 – Fig. 6 with the Fermi energy level indicated by a dotted line in each figure. Fig. 4 revealed that the total DOS values of MoNbTaTiV and MoNbTa<sub>0.5</sub>Ti<sub>1.5</sub>V at Fermi level were all higher than 0, indicating MoNbTaTiV and MoNbTa<sub>0.5</sub>Ti<sub>1.5</sub>V present obvious metallic behavior [44]. The energy corresponding to the double strong peaks flanking the Fermi level was marked in Fig. 4, indicating the presence of a pseudo-energy gap in the alloy. The pseudo energy gap represents the energy difference between the two nearest peaks around the Fermi level, which reflects the covalency of the alloy system [27]. Fig. 4 showed that the pseudo-energy gaps were 1.676 eV for MoNbTaTiV built by SQS, 1.548 eV for MoNbTa<sub>0.5</sub>Ti<sub>1.5</sub>V built by SQS, 2.610 eV for MoNbTaTiV built by SC, 2.558 eV for MoNbTa<sub>0.5</sub>Ti<sub>1.5</sub>V built by SC, 4.209 eV for MoNbTaTiV built by VCA, and 4.008 eV for MoNbTa<sub>0.5</sub>Ti<sub>1.5</sub>V

**Table 3 – The mean elastic constants (C<sub>ij</sub>) and elastic properties of NbMoTaTiV and NbMoTa<sub>0.5</sub>Ti<sub>1.5</sub>V RHEAs.**

Alloy	C <sub>11</sub> (GPa)	C <sub>12</sub> (GPa)	C <sub>44</sub> (GPa)	B(GPa)	G(GPa)	B/G	E(GPa)	$\nu$
NbMoTaTiV-SQS	274.9	125.7	49.7	175.4	58.5	2.997	158.0	0.350
NbMoTa <sub>0.5</sub> Ti <sub>1.5</sub> V-SQS	252.6	122.8	44.2	166.0	51.6	3.221	140.2	0.359
NbMoTaTiV-SC	246.1	132.3	36.7	169.3	42.8	3.960	118.3	0.383
NbMoTa <sub>0.5</sub> Ti <sub>1.5</sub> V-SC	256.6	110.7	28.4	158.9	39.3	4.043	108.9	0.386
NbMoTaTiV-VCA	263.0	148.9	55.2	186.9	56.0	3.338	152.6	0.364
NbMoTa <sub>0.5</sub> Ti <sub>1.5</sub> V-VCA	246.0	145.3	48.0	178.8	48.9	3.657	134.5	0.375
NbMoTaTiV [32]	262.0	141.5	43.2	181.2	50.7	3.574	139.2	0.372

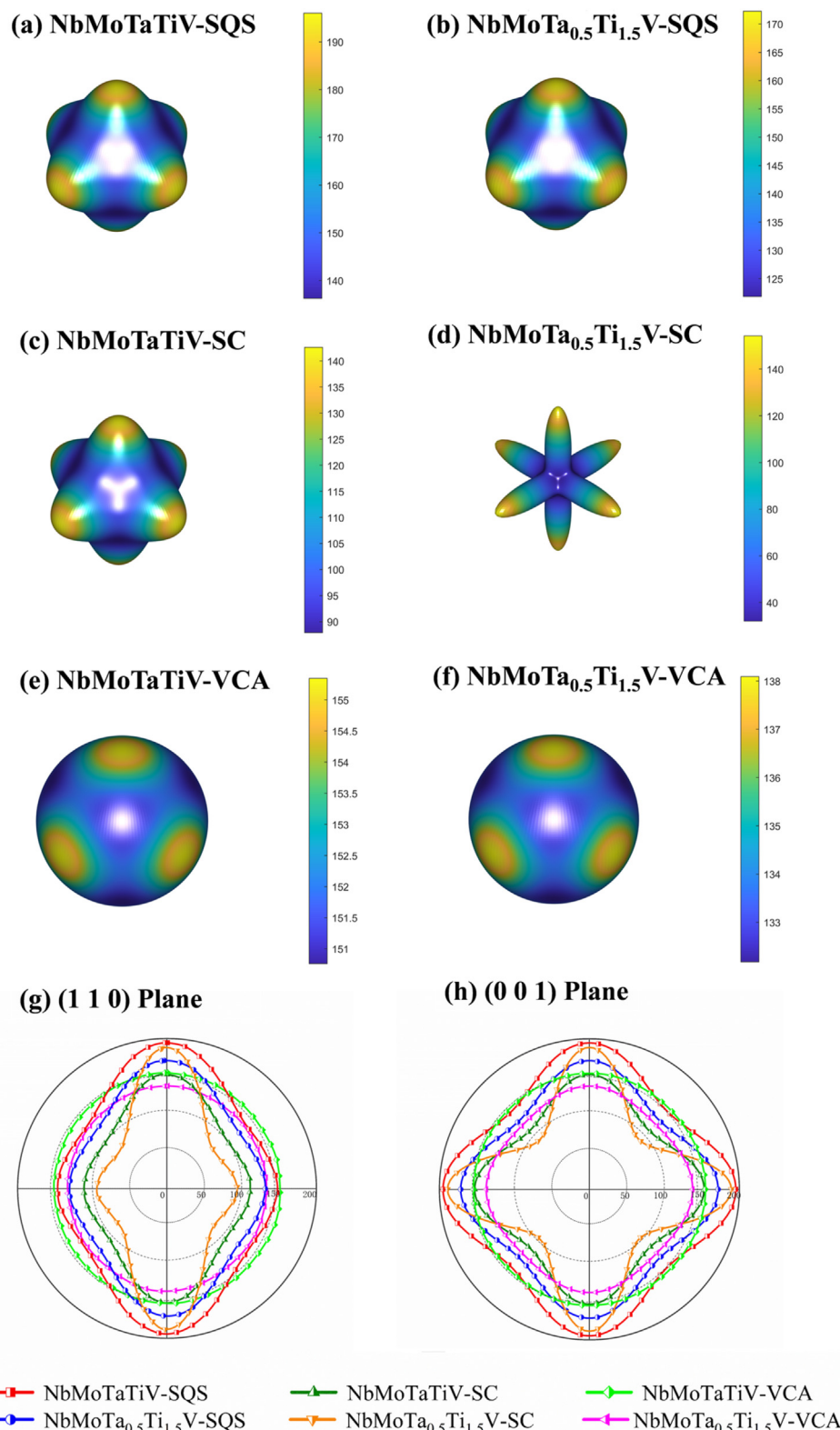


**Fig. 3 – (a)~(d)** 3D diagrams of Yong's modulus' anisotropy for MoNbTaTiV and MoNbTa<sub>0.5</sub>Ti<sub>1.5</sub>V RHEAs built by SQS and VCA; (e)~(f) represent the planar projections of MoNbTaTiV and MoNbTa<sub>0.5</sub>Ti<sub>1.5</sub>V on (110) plan and (001) plan respectively.

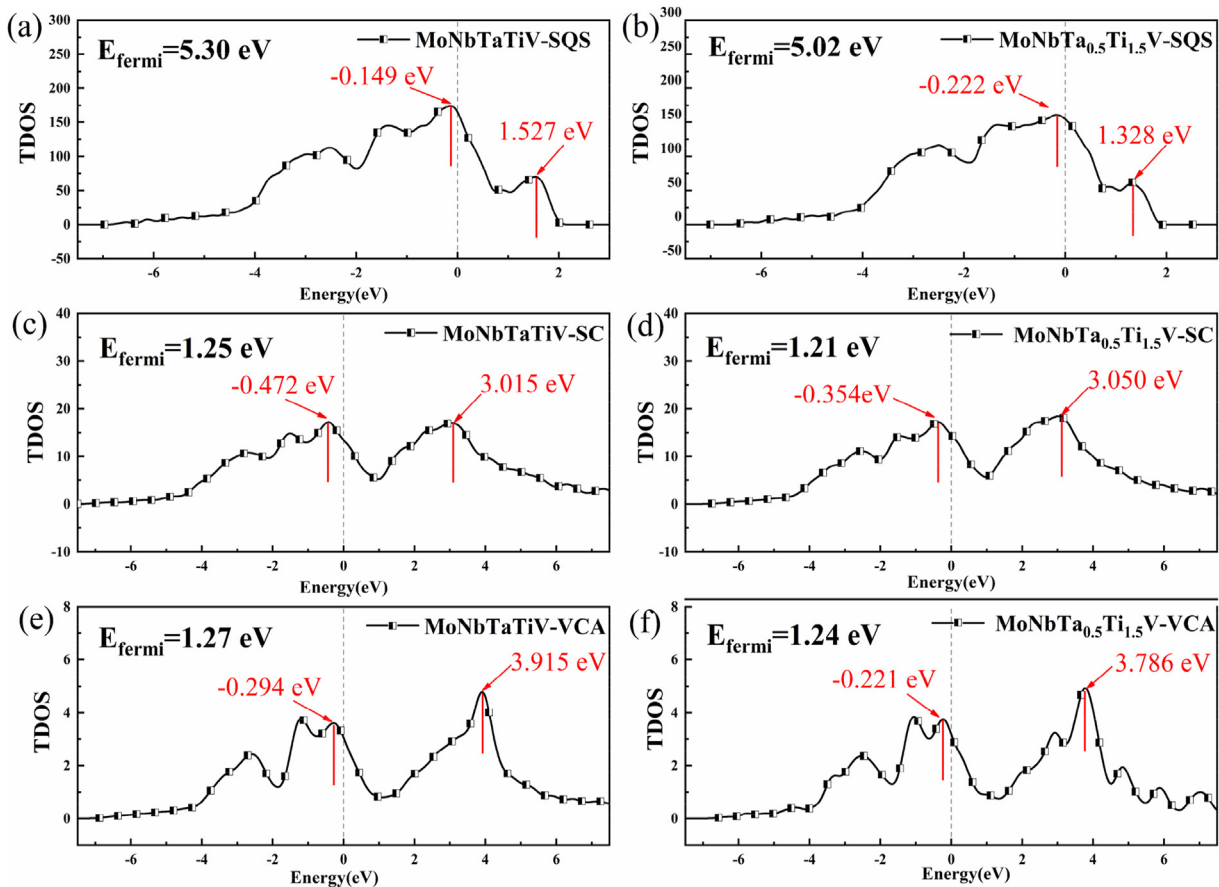


**Fig. 4 – Density of states of MoNbTaTiV and MoNbTa<sub>0.5</sub>Ti<sub>1.5</sub>V built by SQS, SC and VCA. (a)–(b) SQS; (c)–(d) SC; (e)–(f) VCA.**

built by VCA. For the same modeling method, the pseudo-energy gap of MoNbTa<sub>0.5</sub>Ti<sub>1.5</sub>V was small, suggesting that the decrease of Ta content and the increase of Ti weakened the covalency of the alloy system. Additionally, Fermi energy level of MoNbTa<sub>0.5</sub>Ti<sub>1.5</sub>V was low, indicating that with the decrease of Ta element content and the increase of Ti element, more electrons occupied lower energy levels in the alloy system, resulting in a more stable system.

Since the VCA method constructed only one cell, the partial density of states of MoNbTaTiV and MoNbTa<sub>0.5</sub>Ti<sub>1.5</sub>V constructed by the SQS and SC methods are presented in Figs. 5 and 6. Analyzing the partial density of states constructed by the SQS, for MoNbTaTiV, d-orbital electrons of V mainly provided the density of states near the Fermi level, which meant that the metallic properties of the alloy were primarily determined by the V element. For MoNbTa<sub>0.5</sub>Ti<sub>1.5</sub>V, with the increase of Ti, d-orbital electrons of Ti mainly provided the density of states near the Fermi level, signifying that Ti mainly determined the metallicity properties of the alloy. From Fig. 6, it was observed that d-orbital electrons of Ti and V elements mainly provided the density of states near the Fermi level for the MoNbTaTiV built by SC. Similarly, for the MoNbTa<sub>0.5</sub>Ti<sub>1.5</sub>V built by SC, it exhibited a similar pattern to the SQS, d-orbital electrons of Ti mainly provided the density of states near the Fermi level. The PDOS curves of each component have obvious overlap, which indicates that

there is serious electron hybridization among the components, and the covalence in the alloy is strong.

#### 3.4. Experimental validation

To validate the accuracy of the BCC structure modelling, verification of the alloy phase structure was performed. The XRD pattern of the MoNbTaTiV and MoNbTa<sub>0.5</sub>Ti<sub>1.5</sub>V prepared by arc melting were shown in Fig. 7. The XRD patterns confirm that both RHEAs were single-phase BCC phase, which was consistent with the prediction from empirical parameter calculation. Meanwhile, the slight displacement of diffraction peak (110) shown in Fig. 7(b) could reflect the change of lattice constant. The (110) diffraction peak of MoNbTa<sub>0.5</sub>Ti<sub>1.5</sub>V was slightly shifted to the right compared with MoNbTaTiV, which can be attributed to the slightly smaller lattice constant value of Ti (3.276 Å) compared with Ta (3.306 Å). Using the diffraction pattern and Bragg's law, the lattice constants of MoNbTaTiV and MoNbTa<sub>0.5</sub>Ti<sub>1.5</sub>V were determined to be 3.230 Å and 3.226 Å, respectively. In addition, the lattice constants calculated by SQS, SC and VCA were found to be in excellent agreement with the experimental lattice constants. Furthermore, the measured density of MoNbTaTiV and MoNbTa<sub>0.5</sub>Ti<sub>1.5</sub>V samples were 9.29 g/cm<sup>3</sup> and 7.88 g/cm<sup>3</sup>, respectively. The theoretical density calculation was shown in Eq. (6)

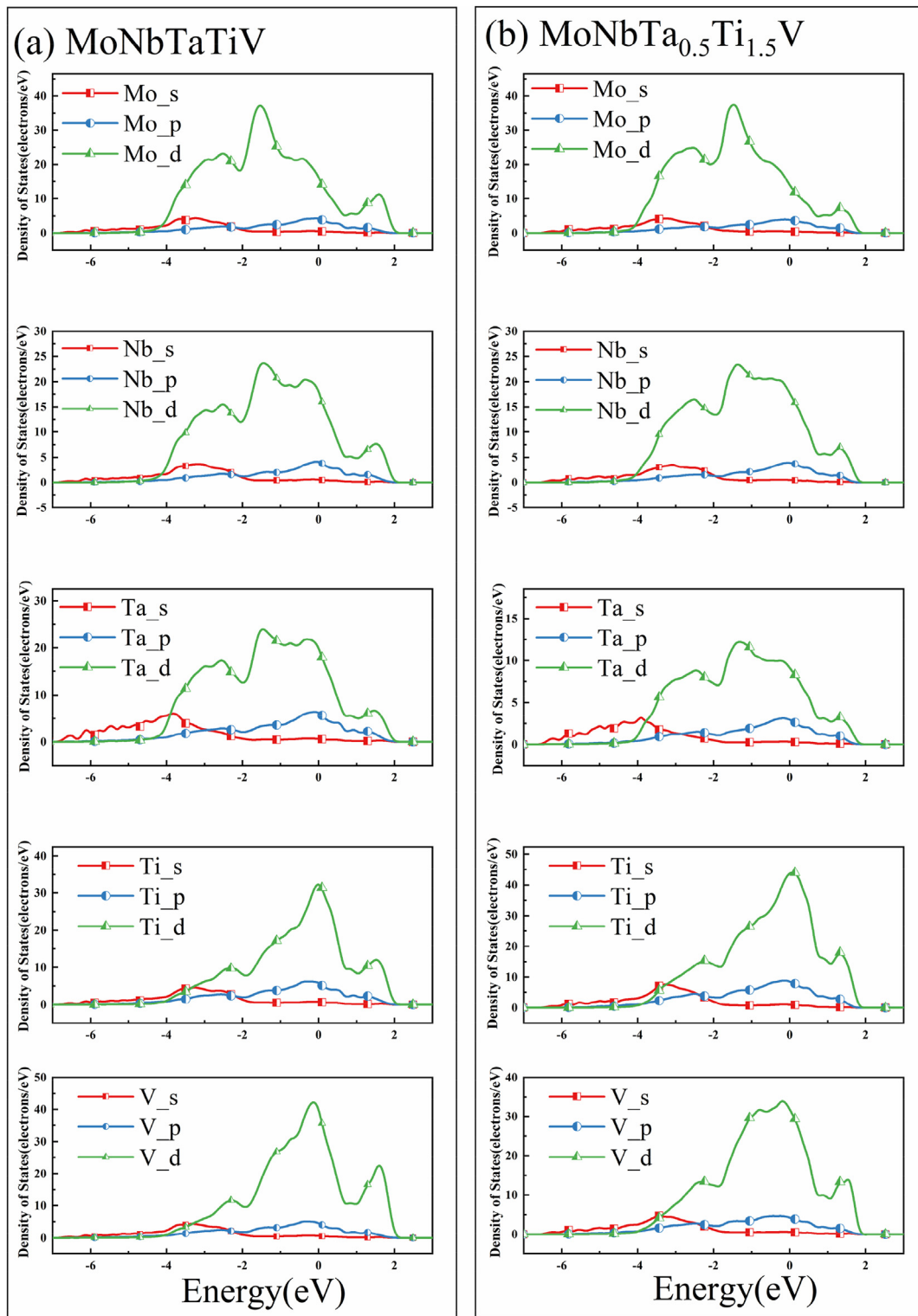


**Fig. 5 – Partial density of states of MoNbTaTiV (a) and MoNbTa<sub>0.5</sub>Ti<sub>1.5</sub>V (b) built by SQS.**

$$\rho = \frac{AM_a + BM_b + CM_c + DM_d + EM_e}{(A + B + C + D + E)N_A a^3} \quad (6)$$

Where,  $N_A$  is the Avogadro constant,  $N_A = 6.022 \times 10^{23}$ ; A, B, C, D and E correspond to the atomic numbers of Mo, Nb, Ta, Ti and V in the modeling cell;  $M_a$ ,  $M_b$ ,  $M_c$ ,  $M_d$  and  $M_e$  represent the relative atomic mass of Mo, Nb, Ta, Ti and V elements;  $a$  is the lattice constant calculated through the first principle calculation by different methods. From Table 4, the calculated density is slightly higher than the measured density. This discrepancy might be attributed to certain defects during the

and V in the modeling cell;  $M_a$ ,  $M_b$ ,  $M_c$ ,  $M_d$  and  $M_e$  represent the relative atomic mass of Mo, Nb, Ta, Ti and V elements;  $a$  is the lattice constant calculated through the first principle calculation by different methods. From Table 4, the calculated density is slightly higher than the measured density. This discrepancy might be attributed to certain defects during the

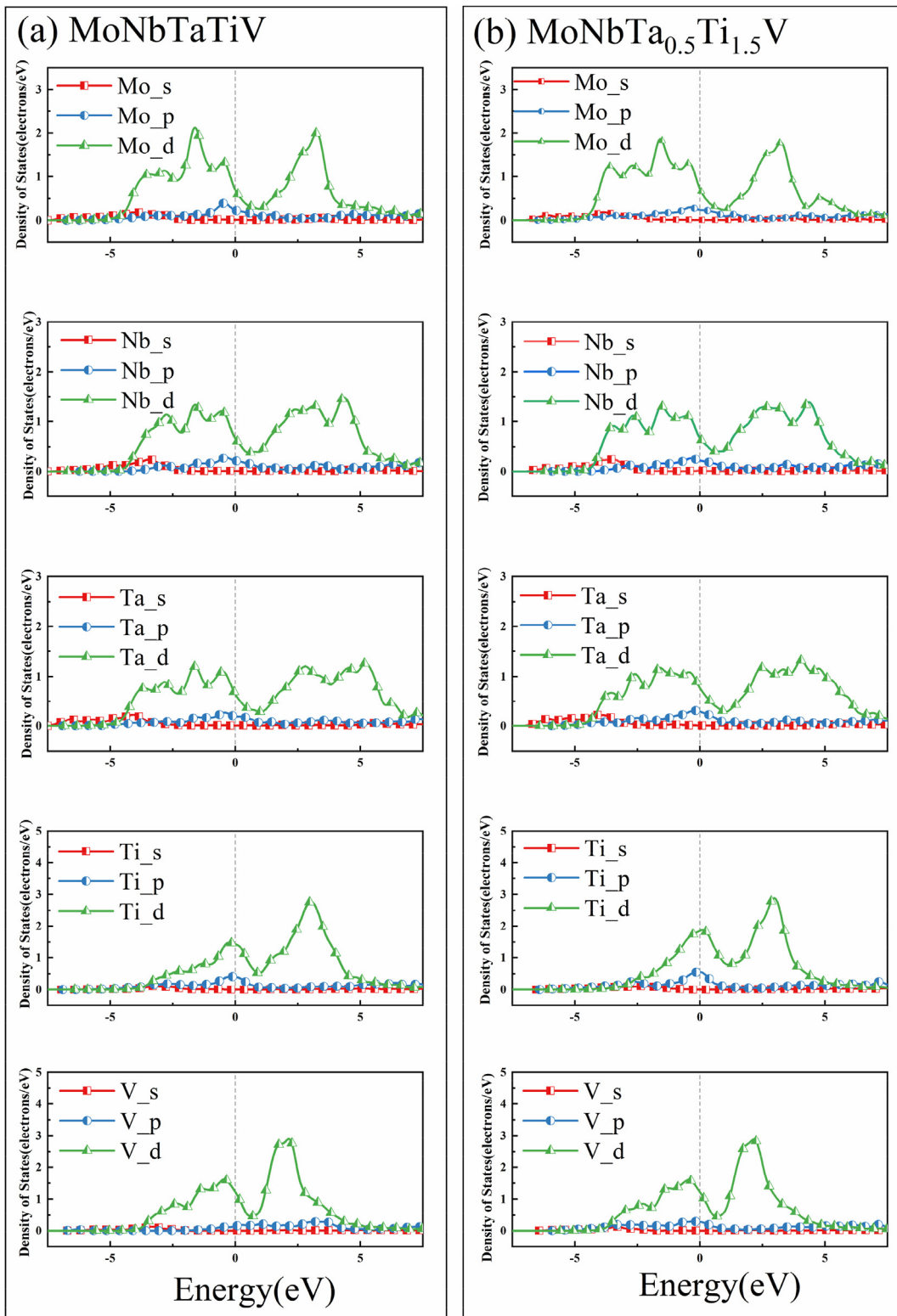


**Fig. 6 – Partial density of states of MoNbTaTiV (a) and MoNbTa<sub>0.5</sub>Ti<sub>1.5</sub>V (b) built by SC.**

arc melting process, such as the formation of pores or vacancy in the cast material.

The SEM images and EDS mapping images of the MoNbTaTiV and MoNbTa<sub>0.5</sub>Ti<sub>1.5</sub>V RHEAs are presented in Fig. 8. The EDS mapping revealed a highly homogeneously

distribution of each constituent element. It was found that the actual measured composition of each element of the MoNbTaTiV and MoNbTa<sub>0.5</sub>Ti<sub>1.5</sub>V RHEAs differed from the nominal design composition by less than 1.2 at%. Considering that EDS is a semi-quantitative method with an error value of about

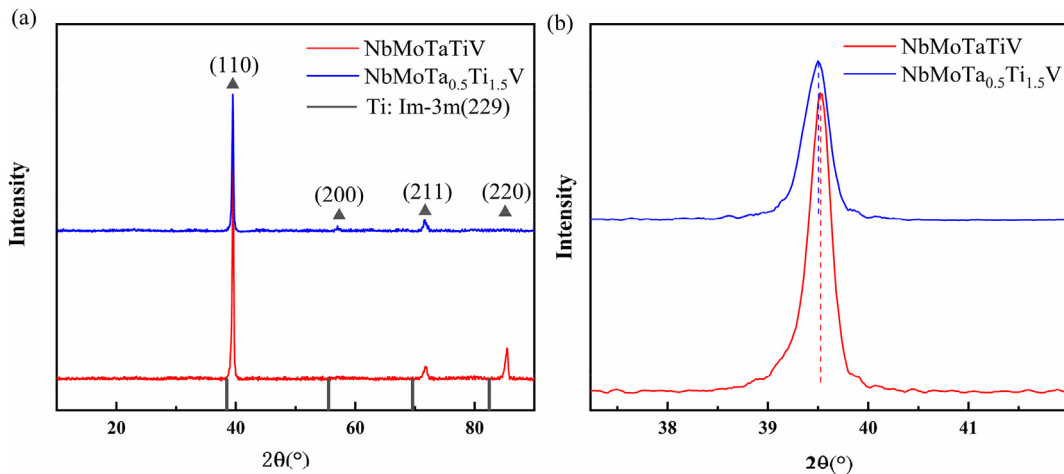


**Fig. 7 – The XRD pattern (a) and the magnified (110) peaks (b) of the MoNbTaTiV and MoNbTa<sub>0.5</sub>Ti<sub>1.5</sub>V.**

±2 at%, it can be inferred that the actual composition of MoNbTaTiV and MoNbTa<sub>0.5</sub>Ti<sub>1.5</sub>V were consistent with the nominal design composition.

Hardness is a critical property that characterizes a material's resistance to localized deformation, serving as an indicator of its mechanical toughness or brittleness. To determine the microhardness of the alloys, the Vickers hardness tester was used to measure the average value at five different points under a 200 g load for 15 s. The Vickers microhardness of MoNbTaTiV and MoNbTa<sub>0.5</sub>Ti<sub>1.5</sub>V were presented in Fig. 9. The theoretical calculated hardness was predicted from shear modulus and bulk modulus based on Chen's model equation as Eq. (7):

$$H_v = 1.887(K^2G)^{0.585}, K = \frac{G}{B} \quad (7)$$

where, G was the shear modulus and B was the bulk modulus.

From Fig. 9, it was evident that the hardness of the RHEAs decreased with the decrease of Ta content and the increase of Ti content. For the model built by SQS, the Chen's model equation does not account for the presence of slip planes, plastic deformation, and lattice defects in the model system. Consequently, the hardness of the model tended to be overestimated compared to the actual experimental results. In addition, the hardness value calculated by SQS method was higher than that calculated by VCA method. This was mainly because the SQS model took into account the distortion caused by the atomic lattice, which would lead to an increase in the hardness of the material. On the other hand, the model built by VCA, which does not consider local atomic positions and lattice distortions, calculated by the Chen's model equation would result in lower estimates than the experimental results. Although the SC model took into account the local atomic positions, the relatively small atomic numbers made it not fully to reflect the material periodicity, resulting the predicted hardness values smaller than the experimental values.

To confirm the precision of the first-principles prediction of elastic properties and Poisson's ratio, a comprehensive experimental investigation was conducted on the RHEAs. The ultrasonic method was utilized to examine the elastic

properties and Poisson's ratio of the MoNbTaTiV and MoNbTa<sub>0.5</sub>Ti<sub>1.5</sub>V RHEA. The UMS ultrasonic technique enabled the evaluation of material characteristics in a non-destructive way and necessitated smaller sized samples. UMS ultrasonic technique calculated the propagation velocity of transverse and longitudinal waves through the material. The density of the material was measured by Archimedes' method. The modulus of elasticity and Poisson's ratio were calculated based on Eqs. (8)–(10):

$$E = \frac{\rho V_t^2 (3V_l^2 - 4V_t^2)}{(V_l^2 - V_t^2)} \quad (8)$$

$$B = \rho \left( V_l^2 - \frac{4}{3} V_t^2 \right) \quad (9)$$

$$\nu = \frac{1 - 2 \left( V_t / V_l \right)^2}{2 - 2 \left( V_t / V_l \right)^2} \quad (10)$$

Where,  $V_t$  and  $V_l$  represent the transverse and longitudinal phonon propagation velocities respectively;  $\rho$  represent the density of the material. The experimental outcomes obtained by the ultrasonic method were shown in Fig. 10. Through UMS experiment verification, it was found that increasing Ti and decreasing Ta could effectively increase the Poisson's ratio of RHEAs and improve the toughness of the alloy, while concurrently reducing the Young's modulus and bulk modulus. This trends were consistent with the first principles results by three different methods.

The room temperature compression engineering stress-strain curves and true stress-strain curves of MoNbTaTiV and MoNbTa<sub>0.5</sub>Ti<sub>1.5</sub>V RHEAs were shown in Fig. 11. The yield strength of MoNbTaTiV and MoNbTa<sub>0.5</sub>Ti<sub>1.5</sub>V RHEAs were 1479 MPa and 1352 MPa, respectively. Comparison with other reported RHEAs' density and compression mechanical properties (as shown in Table 5) indicated that the MoNbTa<sub>0.5</sub>Ti<sub>1.5</sub>V RHEAs studied in this work exhibited relatively favorable strength-to-plasticity matching with low

**Table 4 – The lattice constant and density of MoNbTaTiV and MoNbTa<sub>0.5</sub>Ti<sub>1.5</sub>V RHEAs calculated and experimentally obtained by different methods.**

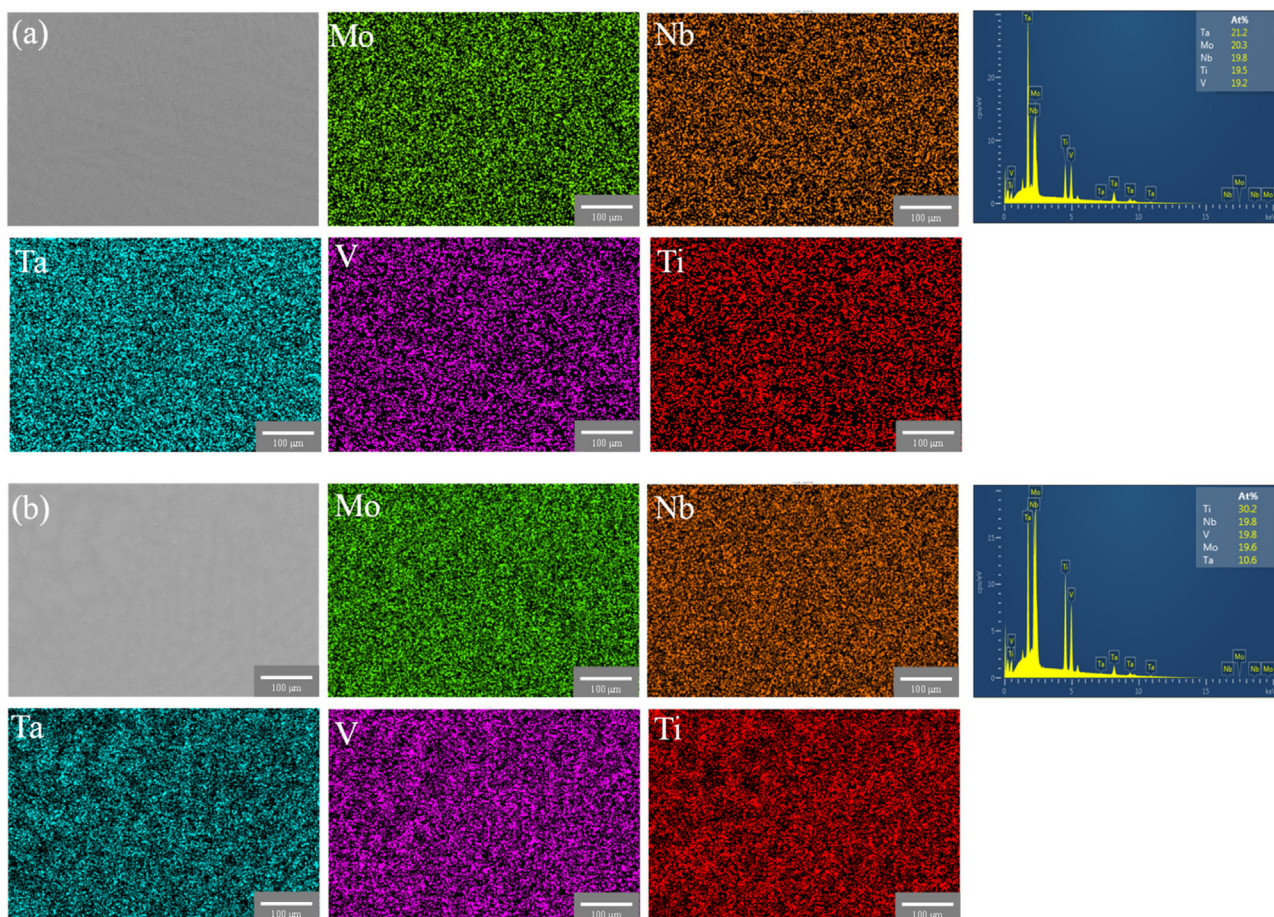
Alloy	Lattice constant (Å)				Density (g/cm <sup>3</sup> )			
	Calculation results-SQS	Calculation results-SC	Calculation results-VCA	Experiment results	Calculation results-SQS	Calculation results-SC	Calculation results-VCA	Experiment results
NbMoTaTiV	3.183	3.221	3.220	3.230	9.65	9.31	9.32	9.29
NbMoTa <sub>0.5</sub> Ti <sub>1.5</sub> V	3.175	3.229	3.210	3.226	8.34	7.93	8.08	7.88

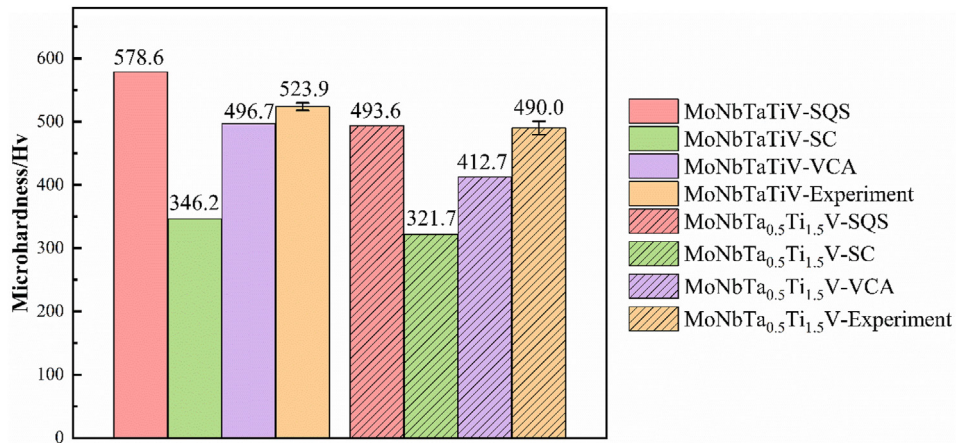
density. The plastic fracture strains of MoNbTaTiV and MoNbTa<sub>0.5</sub>Ti<sub>1.5</sub>V RHEAs were 20% and >50%, respectively. The elastic deformation stage of both MoNbTaTiV and MoNbTa<sub>0.5</sub>Ti<sub>1.5</sub>V RHEAs showed similar curve slopes, albeit with MoNbTaTiV having a slightly higher slope, signifying a slightly larger Young's modulus. These mechanical properties were consistent with those predicted by first principles calculations, further validating the accuracy of the theoretical modeling. In addition, for MoNbTa<sub>0.5</sub>Ti<sub>1.5</sub>V RHEAs, no dramatic stress drop was recorded in the dynamic compression sample after yield, indicating strong resistance to plastic instability. Fig. 11 (b) illustrated the true stress-strain curves of MoNbTaTiV and MoNbTa<sub>0.5</sub>Ti<sub>1.5</sub>V RHEAs, in which the work hardening rate was obtained from the slope of the true stress-strain curves and represented by the dashed line. As the Ti content increases and the Ta content decreases, the ultimate true stress-strain compressive strength of the alloy

increases from 1183 MPa to 1220 MPa. For MoNbTaTiV, the work-hardening rate decreased rapidly to negative values as the strain increases, while the work-hardening rate of MoNbTa<sub>0.5</sub>Ti<sub>1.5</sub>V RHEAs decreased and then remained little changed. The work hardening rate of MoNbTa<sub>0.5</sub>Ti<sub>1.5</sub>V RHEAs fluctuated around 0 after reduction. The more stable work-hardening rate results in better plastic stability for MoNbTa<sub>0.5</sub>Ti<sub>1.5</sub>V. The considerable increase in ductility observed in MoNbTa<sub>0.5</sub>Ti<sub>1.5</sub>V RHEAs was primarily attributed to the alloy's remarkable work-hardening capability.

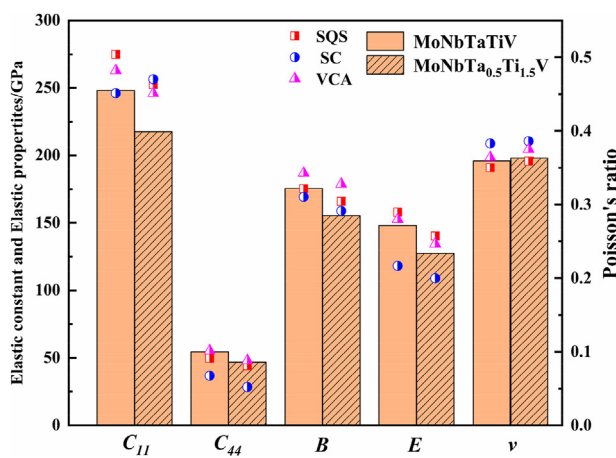
### 3.5. Comparison of different calculation methods

Furthermore, an in-depth analysis of errors and sources of errors of the different modeling methods were performed, as shown in Fig. 12. By comparing the experimental values with the calculated values, it was evident that the calculated built

**Fig. 8 – SEM images and EDS mapping images of the as-cast (a) MoNbTaTiV and (b) MoNbTa<sub>0.5</sub>Ti<sub>1.5</sub>V.**

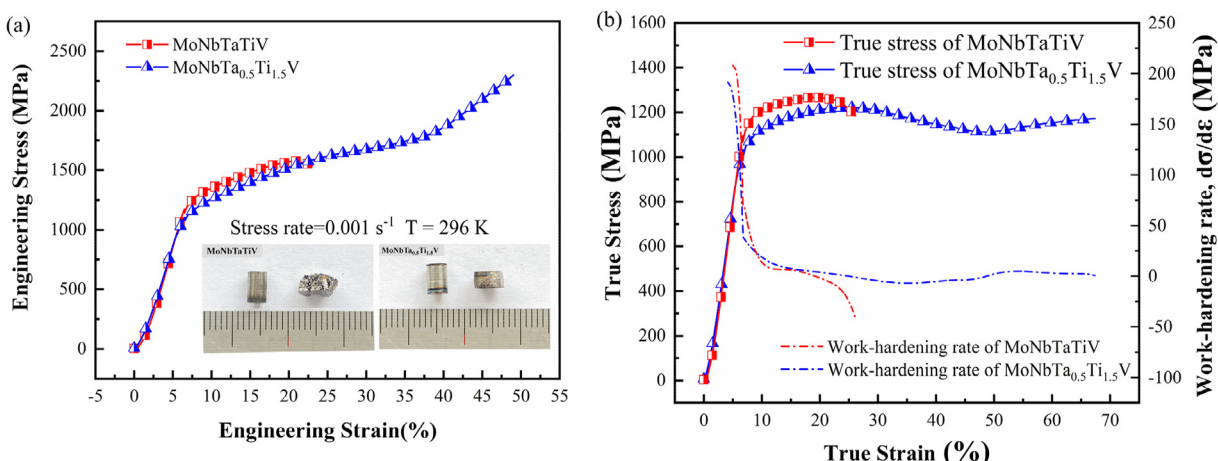


**Fig. 9 – The microhardness of MoNbTaTiV and MoNbTa<sub>0.5</sub>Ti<sub>1.5</sub>V RHEA obtained by the calculation and experiment.**



**Fig. 10 – The Elastic constants, Bulk modulus, Young's modulus and Poisson's ratio of MoNbTaTiV and MoNbTa<sub>0.5</sub>Ti<sub>1.5</sub>V RHEAs by ultrasonic method.**

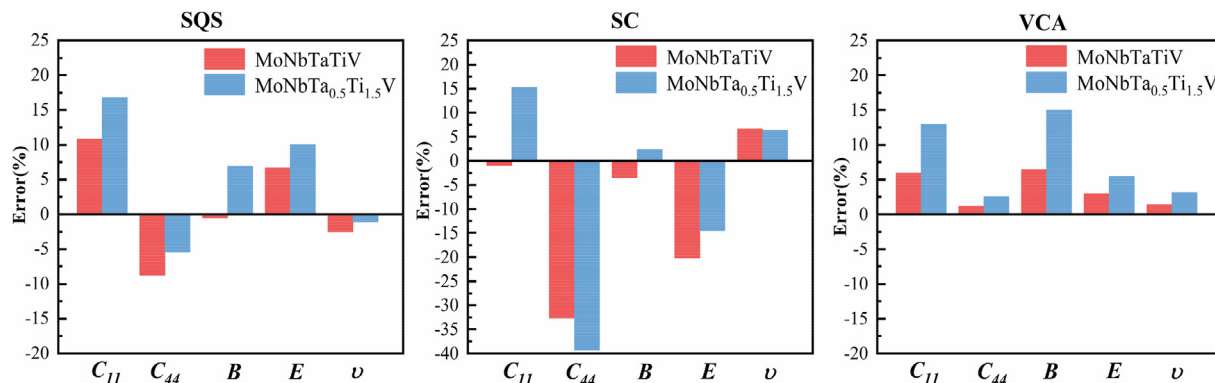
by SQS and VCA methods was closer to the actual measured values. The accuracy of the calculation of elastic constants and elastic properties was VCA > SQS > SC. The significant underestimation of C<sub>44</sub> in the SC modeling method contributed to the larger error values overall. For the SQS modeling approach, it was generally important to ensure that the correlation functions of the first nearest neighbor shell of the supercell were as close as possible to the target random alloy, to ensure the accuracy of the nearest neighbor interactions. The crystal symmetry of the supercell was usually broken to accommodate the required correlation functions between different elements. Both the size of the supercell and the degree of fit of the correlation function were critical factors influencing the calculation results. On the other hand, since the HEA was short-range random and the occupancy of its atoms in the lattice was not clear, the SC modeling method involved artificial random substitution with a certain degree of randomness, making the calculation error larger. As for VCA modeling method, the errors of VCA were all positive, which means that the calculated values were generally high.



**Fig. 11 – Engineering stress–strain curves and of the MoNbTaTiV and MoNbTa<sub>0.5</sub>Ti<sub>1.5</sub>V RHEA obtained from compressive tests under room temperature.**

**Table 5 – The density and compressive mechanical properties of MoNbTaTiV, MoNbTa<sub>0.5</sub>Ti<sub>1.5</sub>V RHEAs and other RHEAs reported in the literature.**

Alloys	Density (g/cm <sup>3</sup> )	Yield strength (MPa)	Fracture strain (%)	Refs.
MoNbTaTiV	9.29	1479	20	This work
MoNbTa <sub>0.5</sub> Ti <sub>1.5</sub> V	7.88	1352	>50	This work
NbMoTaW	13.75	1058	0.95	[16]
NbMoTaWV	12.36	1246	1.7	[16]
HfMoTaTiZr	10.24	1600	4	[45]
NbCrMo <sub>0.5</sub> Ta <sub>0.5</sub> TiZr	8.23	1595	5	[19]
MoNbHfZrTi	~	1719	10.12	[46]
AlMo <sub>0.5</sub> NbTa <sub>0.5</sub> TiZr	7.4	2197	4.1	[47]
AlMo <sub>0.5</sub> NbTa <sub>0.5</sub> TiZr <sub>0.5</sub>	7.4	—	1.0	[47]
AlNbTa <sub>0.5</sub> TiZr <sub>0.5</sub>	7.1	1352	1.3	[47]
Al <sub>0.5</sub> Mo <sub>0.5</sub> NbTa <sub>0.5</sub> TiZr	8.1	2350	3.2	[47]
Al <sub>0.25</sub> NbTaTiZr	9.4	1745	3.8	[47]
AlNbTiZr	5.85	1579	17.8	[48]
WTaMoNbTi	~	1457	7.8	[49]
WReTaMo	~	1075	5.1	[50]
CrNbTiZr	6.67	1260	6	[51]
CrNbTiVZr	6.57	1298	6	[51]
HfMoScTaZr	9.28	1778	27	[52]

**Fig. 12 – The error of MoNbTaTiV and MoNbTa<sub>0.5</sub>Ti<sub>1.5</sub>V RHEAs by different methods.**

compared with the experiment results. Although VCA method cannot realistically reflect the lattice distortion and elemental undulations of HEAs, it was suitable for calculating the average properties of the alloy. The UMS test measured the bulk properties of the material on a relatively large scale, not on the micro-nanometer scale. Therefore, in this case, the VCA calculation was closer to the experimental value.

From the perspective of computational efficiency, VCA method ignored the influence of local atomic environment on the system, which significantly improved computational efficiency. However, both SC and SQS required to build supercells, and the computational efficiency was positively correlated with the number of atoms. In this paper, the computational efficiency was VCA > SC > SQS. Considering both calculation accuracy and efficiency, VCA method was more suitable for predicting elastic properties. Meanwhile, SQS and SC considered the complex atomic occupation in HEAs which were better suited for the study of the electronic structure and can calculate the electronic density of state, band structure and stacking fault energy and so on.

#### 4. Conclusion

In this study, the structural and mechanical properties of NbMoTaTiV and NbMoTa<sub>0.5</sub>Ti<sub>1.5</sub>V were investigated using a combination of first principle calculations and experimental verification. The goal was to enhance the toughness and reduce the density of these alloys in comparison to MoNbTaTiV RHEA, achieved through an intentional increase in Ti content and decrease in Ta content. The phase structure, formation enthalpy, cohesive energy, elastic properties and electronic structure of MoNbTaTiV and MoNbTa<sub>0.5</sub>Ti<sub>1.5</sub>V RHEAs were predicted by first-principle calculation built by three common modeling methods: SQS, SC and VCA. Both theoretical criterion calculation and experimental verification confirmed that MoNbTaTiV and MoNbTa<sub>0.5</sub>Ti<sub>1.5</sub>V RHEAs have BCC single-phase solid solution structure. First principle calculations predict that both MoNbTaTiV and MoNbTa<sub>0.5</sub>Ti<sub>1.5</sub>V RHEAs have electrically conductive and metallic properties. Through UMS experiment verification of vacuum arc melting samples, it was found that increasing Ti and decreasing Ta

could indeed improve the Poisson's ratio of RHEAs, enhancing the toughness of the alloy while reducing the Young's modulus and bulk modulus. Room temperature compression experiments have demonstrated that increasing Ti and decreasing Ta could improve the room temperature plasticity of the RHEAs from 20% to >50%. Importantly, the increase in plasticity was accompanied by a reduction in material density. In addition, three modeling methods are compared from error sources and computational efficiency. Based on UMS test was the measurement of the bulk properties of the material, VCA method was more suitable for predicting elastic properties, offered a combination of high calculation accuracy and efficiency. On the other hand, SQS and SC considered the complex atomic occupation in HEAs which were more appropriate for studying electronic structure. This work indicates that first principle calculation using SQS, SC and VCA were both effective methods and promising research approaches to predict the properties of RHEAs.

## Data availability

The raw/processed data required to reproduce these findings cannot be shared at this time as the data also forms part of an ongoing study.

## Declaration of Competing Interest

We declare that we have no financial and personal relationships with other people or organizations that can inappropriately influence our work.

## Acknowledgements

This work was supported by Natural Science Foundation of Guangdong Province [grant number 2023A1515011436].

## REFERENCES

- [1] Yeh Jien-Wei, Chen Swe-Kai, Lin Su-Jien, Gan Jon-Yiew, Chin Tsung-Shune, Shun Tao-Tsung, et al. Nanostructured high-entropy alloys with multiple principal elements: novel alloy design concepts and outcomes. *Adv Eng Mater* 2004;6:299–303. <https://doi.org/10.1002/adem.200300567>.
- [2] Cantor B, Chang ITH, Knight P, Vincent AJB. Microstructural development in equiatomic multicomponent alloys. *Mater Sci Eng* 2004;375–377:213–8. <https://doi.org/10.1016/j.msea.2003.10.257>.
- [3] Yeh JW. Recent progress in high-entropy alloys, vol. 31. Annales De Chimie-Science Des Materiaux; 2006. p. 633–48. <https://doi.org/10.3166/acsm.31.633-648>.
- [4] Zhang Y, Zuo TT, Tang Z, Gao MC, Dahmen KA, Liaw PK, et al. Microstructures and properties of high-entropy alloys. *Prog Mater Sci* 2014;61:1–93. <https://doi.org/10.1016/j.jpmatsci.2013.10.001>.
- [5] Borkar T, Gwalani B, Choudhuri D, Mikler CV, Yannetta CJ, Chen X, et al. A combinatorial assessment of AlxCrCuFeNi<sub>2</sub> (0 < x < 1.5) complex concentrated alloys: microstructure, microhardness, and magnetic properties. *Acta Mater* 2016;116:63–76. <https://doi.org/10.1016/j.actamat.2016.06.025>.
- [6] Tan XR, Zhao RF, Ren B, Zhi Q, Zhang GP, Liu ZX. Effects of hot pressing temperature on microstructure, hardness and corrosion resistance of Al2NbTi3V2Zr high-entropy alloy. *Mater Sci Technol* 2016;32:1582–91. <https://doi.org/10.1080/02670836.2015.1132548>.
- [7] Alaneme KK, Bodunrin MO, Oke SR. Processing, alloy composition and phase transition effect on the mechanical and corrosion properties of high entropy alloys: a review. *J Mater Res Technol* 2016;5:384–93. <https://doi.org/10.1016/j.jmrt.2016.03.004>.
- [8] Huang K, Chen L, Lin X, Huang H, Tang S, Du F. Wear and corrosion resistance of Al0.5CoCrCuFeNi high-entropy alloy coating deposited on AZ91D magnesium alloy by laser cladding. *Entropy* 2018;20:915. <https://doi.org/10.3390/e20120915>.
- [9] Mathiou C, Poulia A, Georgatis E, Karantzalis AE. Microstructural features and dry - sliding wear response of MoTaNbZrTi high entropy alloy. *Mater Chem Phys* 2018;210:126–35. <https://doi.org/10.1016/j.matchemphys.2017.08.036>.
- [10] Ge F, Yuan H, Gao Q, Peng T, Guo S, Lyu P, et al. Microstructure, hardness and wear resistance of AlCoCrFeNiTax (x = 0, 0.1, 0.3) high-entropy alloys enhanced by laser remelting and Ta addition. *J Alloys Compd* 2023;949. <https://doi.org/10.1016/j.jallcom.2023.169741>.
- [11] Shi H, Tang C, Jianu A, Fetzer R, Weisenburger A, Steinbrueck M, et al. Oxidation behavior and microstructure evolution of alumina-forming austenitic & high entropy alloys in steam environment at 1200 °C. *Corrosion Sci* 2020;170:108654. <https://doi.org/10.1016/j.corsci.2020.108654>.
- [12] Ouyang D, Chen Z-j, Yu H-b, Chan KC, Liu L. Oxidation behavior of the Ti38V15Nb23Hf24 refractory high-entropy alloy at elevated temperatures. *Corrosion Sci* 2022;198:110153. <https://doi.org/10.1016/j.corsci.2022.110153>.
- [13] Wang C, Yu J, Yu Y, Zhao Y, Zhang Y, Han X. Comparison of the corrosion and passivity behavior between CrMnFeCoNi and CrFeCoNi coatings prepared by argon arc cladding. *J Mater Res Technol* 2020;9:8482–96. <https://doi.org/10.1016/j.jmrt.2020.05.093>.
- [14] Miracle DB, Senkov ON. A critical review of high entropy alloys and related concepts. *Acta Mater* 2017;122:448–511. <https://doi.org/10.1016/j.actamat.2016.08.081>.
- [15] Senkov ON, Wilks GB, Miracle DB, Chuang CP, Liaw PK. Refractory high-entropy alloys. *Intermetallics* 2010;18:1758–65. <https://doi.org/10.1016/j.intermet.2010.05.014>.
- [16] Senkov ON, Wilks GB, Scott JM, Miracle DB. Mechanical properties of Nb25Mo25Ta25W25 and V20Nb20Mo20Ta20W20 refractory high entropy alloys. *Intermetallics* 2011;19:698–706. <https://doi.org/10.1016/j.intermet.2011.01.004>.
- [17] Senkov ON, Miracle DB, Chaput KJ, Couzinie J-P. Development and exploration of refractory high entropy alloys—a review. *J Mater Res* 2018;33:3092–128. <https://doi.org/10.1557/jmr.2018.153>.
- [18] Senkov ON, Scott JM, Senkova SV, Miracle DB, Woodward CF. Microstructure and room temperature properties of a high-entropy TaNbHfZrTi alloy. *J Alloys Compd* 2011;509:6043–8. <https://doi.org/10.1016/j.jallcom.2011.02.171>.
- [19] Senkov ON, Woodward CF. Microstructure and properties of a refractory NbCrMo0.5Ta0.5TiZr alloy. *Materials Science And Engineering a-Structural Materials Properties Microstructure And Processing* 2011;529:311–20. <https://doi.org/10.1016/j.msea.2011.09.033>.
- [20] Maiti S, Steurer W. Structural-disorder and its effect on mechanical properties in single-phase TaNbHfZr high-

- entropy alloy. *Acta Mater* 2016;106:87–97. <https://doi.org/10.1016/j.actamat.2016.01.018>.
- [21] Guo Z, Zhang A, Han J, Meng J. Effect of Si additions on microstructure and mechanical properties of refractory NbTaWMo high-entropy alloys. *J Mater Sci* 2019;54:5844–51. <https://doi.org/10.1007/s10853-018-03280-z>.
- [22] Senkov ON, Scott JM, Senkova SV, Meisenkothen F, Miracle DB, Woodward CF. Microstructure and elevated temperature properties of a refractory TaNbHfZrTi alloy. *J Mater Sci* 2012;47:4062–74. <https://doi.org/10.1007/s10853-012-6260-2>.
- [23] Gao Y, Qiao L, Wu D, Zhang Y, Zou Y. First principle calculation of the effect of Cr, Ti content on the properties of VMoNbTaWMx ( $M = Cr, Ti$ ) refractory high entropy alloy. *Vacuum* 2020;179:109459. <https://doi.org/10.1016/j.vacuum.2020.109459>.
- [24] Chen L, Hao X, Wang Y, Zhang X, Liu H. First-principles calculation of the effect of Ti content on the structure and properties of TiVNbMo refractory high-entropy alloy. *Mater Res Express* 2020;7:106516. <https://doi.org/10.1088/2053-1591/abbf11>.
- [25] Tian L-Y, Wang G, Harris JS, Irving DL, Zhao J, Vitos L. Alloying effect on the elastic properties of refractory high-entropy alloys. *Mater Des* 2017;114:243–52. <https://doi.org/10.1016/j.matdes.2016.11.079>.
- [26] Mo J-Y, Wan Y-X, Zhang Z-B, Wang X, Li X-Q, Shen B-L, et al. First-principle prediction of structural and mechanical properties in NbMoTaWRex refractory high-entropy alloys with experimental validation. *Rare Metals*; 2022. <https://doi.org/10.1007/s12598-022-02054-6>.
- [27] Hu YL, Bai LH, Tong YG, Deng DY, Liang XB, Zhang J, et al. First-principle calculation investigation of NbMoTaW based refractory high entropy alloys. *J Alloys Compd* 2020;827:153963. <https://doi.org/10.1016/j.jallcom.2020.153963>.
- [28] Tong Y, Bai L, Liang X, Hua M, Liu J, Li Y, et al. Mechanical performance of  $(NbTaW)_{1-x}Mo_x$  ( $x = 0, 0.05, 0.15, 0.25$ ) refractory high entropy alloys: perspective from experiments and first principles calculations. *J Alloys Compd* 2021;873:159740. <https://doi.org/10.1016/j.jallcom.2021.159740>.
- [29] Bai L, Hu Y, Liang X, Tong Y, Liu J, Zhang Z, et al. Titanium alloying enhancement of mechanical properties of NbTaMoW refractory high-Entropy alloy: first-principles and experiments perspective. *J Alloys Compd* 2021;857:157542. <https://doi.org/10.1016/j.jallcom.2020.157542>.
- [30] Liu H, Liu L, Xin C. Effect of alloying elements on the structure and mechanical properties of NbMoTaWX ( $X = Cr, V, Ti, Zr$ , and  $Hf$ ) refractory high-entropy alloys. *AIP Adv* 2021;11:025044. <https://doi.org/10.1063/5.0038405>.
- [31] Bhandari U, Zhang C, Zeng C, Guo S, Yang S. Computational and experimental investigation of refractory high entropy alloy Mo15Nb20Re15Ta30W20. *J Mater Res Technol* 2020;9:8929–36. <https://doi.org/10.1016/j.jmrt.2020.06.036>.
- [32] Yao HW, Qiao JW, Hawk JA, Zhou HF, Chen MW, Gao MC. Mechanical properties of refractory high-entropy alloys: experiments and modeling. *J Alloys Compd* 2017;696:1139–50. <https://doi.org/10.1016/j.jallcom.2016.11.188>.
- [33] Gao Y, Bai S, Chong K, Liu C, Cao Y, Zou Y. Machine learning accelerated design of non-equiaatomic refractory high entropy alloys based on first principles calculation. *Vacuum* 2023;207. <https://doi.org/10.1016/j.vacuum.2022.111608>.
- [34] Zhang Y, Zhou YJ, Lin JP, Chen GL, Liaw PK. Solid-solution phase formation rules for multi-component alloys. *Adv Eng Mater* 2008;10:534–8. <https://doi.org/10.1002/adem.200700240>.
- [35] Guo S, Liu CT. Phase stability in high entropy alloys: formation of solid-solution phase or amorphous phase. *Prog Nat Sci: Mater Int* 2011;21:433–46. [https://doi.org/10.1016/s1002-0071\(12\)60080-x](https://doi.org/10.1016/s1002-0071(12)60080-x).
- [36] Guo S, Ng C, Lu J, Liu CT. Effect of valence electron concentration on stability of fcc or bcc phase in high entropy alloys. *J Appl Phys* 2011;109:5. <https://doi.org/10.1063/1.3587228>.
- [37] Chen R, Qin G, Zheng H, Wang L, Su Y, Chiu Y, et al. Composition design of high entropy alloys using the valence electron concentration to balance strength and ductility. *Acta Mater* 2018;144:129–37. <https://doi.org/10.1016/j.actamat.2017.10.058>.
- [38] Miedema A, Deboer F, Boom R. Model predictions for enthalpy of formation of transition-metal alloys. *Calphad-Computer Coupling Of Phase Diagrams And Thermochemistry* 1977;1:341–59.
- [39] Yang X, Zhang Y. Prediction of high-entropy stabilized solid-solution in multi-component alloys. *Mater Chem Phys* 2012;132:233–8. <https://doi.org/10.1016/j.matchemphys.2011.11.021>.
- [40] Chang S-Y, Chen D-S. Ultrathin  $(AlCrTaTiZr)N[x]/AlCrTaTiZr$  bilayer structures with high diffusion resistance for Cu interconnects. *J Electrochem Soc* 2010;157:G154. <https://doi.org/10.1149/1.3374194>.
- [41] Gao MC, Alman DE. Searching for next single-phase high-entropy alloy compositions. *Entropy* 2013;15:4504–19. <https://doi.org/10.3390/e15104504>.
- [42] Yao X-J, Shi X-F, Wang Y-P, Gan G-Y, Tang B-Y. The mechanical properties of high entropy (-like) alloy  $W-x(TaTiVCr)(1-x)$  via first-principles calculations. *Fusion Eng Des* 2018;137:35–42. <https://doi.org/10.1016/j.fusengdes.2018.08.008>.
- [43] Pugh SF, XCII. Relations between the elastic moduli and the plastic properties of polycrystalline pure metals. London, Edinburgh Dublin Phil Mag J Sci 2009;45:823–43. <https://doi.org/10.1080/14786440808520496>.
- [44] Nong Z-s, Zhu J-c, Yu H-l, Lai Z-h. First principles calculation of intermetallic compounds in FeTiCoNiVCrMnCuAl system high entropy alloy. *Trans Nonferrous Metals Soc China* 2012;22:1437–44. [https://doi.org/10.1016/s1003-6326\(11\)61338-1](https://doi.org/10.1016/s1003-6326(11)61338-1).
- [45] Juan C-C, Tsai M-H, Tsai C-W, Lin C-M, Wang W-R, Yang C-C, et al. Enhanced mechanical properties of HfMoTaTiZr and HfMoNbTaTiZr refractory high-entropy alloys. *Intermetallics* 2015;62:76–83. <https://doi.org/10.1016/j.intermet.2015.03.013>.
- [46] Guo NN, Wang L, Luo LS, Li XZ, Su YQ, Guo JJ, et al. Microstructure and mechanical properties of refractory MoNbHfZrTi high-entropy alloy. *Mater Des* 2015;81:87–94. <https://doi.org/10.1016/j.matdes.2015.05.019>.
- [47] Senkov ON, Jensen JK, Pilchak AL, Miracle DB, Fraser HL. Compositional variation effects on the microstructure and properties of a refractory high-entropy superalloy  $AlMo_0.5NbTa_0.5TiZr$ . *Mater Des* 2018;139:498–511. <https://doi.org/10.1016/j.matdes.2017.11.033>.
- [48] Chen W, Tang QH, Wang H, Xie YC, Yan XH, Dai PQ. Microstructure and mechanical properties of a novel refractory  $AlNbTiZr$  high-entropy alloy. *Mater Sci Technol* 2018;34:1309–15. <https://doi.org/10.1080/02670836.2018.1446267>.
- [49] Wan Y, Mo J, Wang X, Zhang Z, Shen B, Liang X. Mechanical properties and phase stability of WTaMoNbTi refractory high-entropy alloy at elevated temperatures. *Acta Metall Sinica-Engl Lett* 2021;34(11):1585–90. <https://doi.org/10.1007/s40195-021-01263-9>.

- [50] Wan Y, Wang Q, Mo J, Zhang Z, Wang X, Liang X, et al. WReTaMo refractory high-entropy alloy with high strength at 1600 °C. *Adv Eng Mater* 2021;24. <https://doi.org/10.1002/adem.202100765>.
- [51] Senkov ON, Senkova SV, Miracle DB, Woodward C. Mechanical properties of low-density, refractory multi-principal element alloys of the Cr-Nb-Ti-V-Zr system. *Materials Science And Engineering a-Structural Materials Properties Microstructure And Processing* 2013;565:51–62. <https://doi.org/10.1016/j.msea.2012.12.018>.
- [52] Nie XW, Cai MD, Cai S. Microstructure and mechanical properties of a novel refractory high entropy alloy HfMoScTaZr. *Int J Refract Metals Hard Mater* 2021;98:105568. <https://doi.org/10.1016/j.ijrmhm.2021.105568>.